

Article

Widespread Decline in Vegetation Photosynthesis in Southeast Asia Due to the Prolonged Drought During the 2015/2016 El Niño

Xin Qian ^{1,2}, Bo Qiu ^{1,2,*} and Yongguang Zhang ^{1,2}

¹ Jiangsu Provincial Key Laboratory of Geographic Information Science and Technology, International Institute for Earth System Science, Nanjing University, Nanjing 210023, China; mg1627067@mail.nju.edu.cn (X.Q.); yongguang_zhang@nju.edu.cn (Y.Z.)

² Jiangsu Center for Collaborative Innovation in Geographic Information Resource Development and Application, Nanjing 210023, China

* Correspondence: qiubo@nju.edu.cn

Received: 6 March 2019; Accepted: 9 April 2019; Published: 14 April 2019



Abstract: El Niño events are known to be associated with climate extremes and have substantial impacts on the global carbon cycle. The drought induced by strong El Niño event occurred in the tropics during 2015 and 2016. However, it is still unclear to what extent the drought could affect photosynthetic activities of crop and forest in Southeast Asia. Here, we used the satellite solar-induced chlorophyll fluorescence (SIF), which is a proxy of actual photosynthesis, along with traditional vegetation indices (Enhanced Vegetation Index, EVI) and total water storage to investigate the impacts of El Niño-induced droughts on vegetation productivity of the forest and crop in the Southeast Asia. We found that SIF was more sensitive to the water stress than traditional vegetation indices (EVI) to monitor drought for both evergreen broadleaf forest and croplands in Southeast Asia. The higher solar radiation partly offset the negative effects of droughts on the vegetation productivity, leading to a larger decrease of SIF yield (SIF_{yield}) than SIF. Therefore, SIF_{yield} had a larger reduction and was more sensitive to precipitation deficit than SIF during the drought. The comparisons of retrieved column-average dry-air mole fraction of atmospheric carbon dioxide with SIF demonstrated the reduction of CO_2 uptake by vegetation in Southeast Asia during the drought. This study highlights that SIF is more beneficial than EVI to be an indicator to characterize and monitor the dynamics of drought in tropical vegetated regions.

Keywords: solar-induced chlorophyll fluorescence; extreme climatic events; photosynthesis; drought; El Niño events

1. Introduction

Observation and terrestrial biosphere modelling studies have demonstrated the strong impacts of extreme climatic events on terrestrial ecosystem carbon cycle [1–3]. The years of 2015/16 experienced one of the strongest El Niño events since the 1950s, which led to historic warm and dry conditions over the tropical region. This El Niño event has likely caused the historically high atmospheric CO_2 growth rate over 3 ppm year⁻¹ in 2015 and 2016 [4]. Subsequently, the historic warm and dry conditions resulted in widespread droughts globally, with greatest severity over regions including Amazon, central Europe, north China and Southeast Asia [5–8]. Drought can have adverse impacts on both ecosystems and human society, such as regional agriculture and water resources. In Southeast Asia, severe drought associated with this monster El Niño event has caused a severe impact on crop production in Vietnam and Thailand [9]. In particular, the extended dry conditions in Indonesia led to widespread forest and peatland fires and largest carbon emissions in 2015 in the Southeast Asia

since 1997 [6]. The ocean-atmosphere events e.g., El-Niño and the Madden-Julian Oscillation (MJO), have substantial influence on extreme dry/wet conditions, which is associated with air temperature and precipitation [10].

Many efforts have been made to develop various quantitative measures for accurate monitoring of drought extent and severity [11]. Satellite observations of vegetation status, with its global coverage, provide useful information to monitor the spatiotemporal changes of vegetation in response to drought at broad scales, and thus improve simulations of carbon fluxes of terrestrial ecosystems. Since droughts are associated with vegetation state and coverage, greenness-based vegetation indices (VIs), such as normalized difference vegetation index (NDVI), have been widely used for drought monitoring [12]. Based on NDVI, several drought indices have been developed for regional to global scale drought assessment [11,13]. Some other VIs, such as the enhanced vegetation index (EVI) [14], has been also widely used to monitor the vegetation response to drought in the Amazon [15] and in central Africa [16]. EVI has less saturation problems over dense forest area than other greenness index. However, the greenness-based VIs only indicates potential photosynthesis and relates to vegetation functioning indirectly. Furthermore, saturation of VIs in dense canopies of tropical forests leads to a lack of sensitivity to detect the stress-induced degradation in the forest canopy. Therefore, it has been suggested that greenness-based VIs are not sufficient to capture the dynamic response of vegetation to varying water stress [17].

In this regard, for stress detection, chlorophyll fluorescence (ChlF) is especially useful as a non-destructive probe, and has been used to investigate the plant response to water stress at leaf and canopy scales on the ground [18]. ChlF is an emission in the 650–800 nm range originating at the core of the photosynthetic machinery after light absorption [19], and the ChlF emission has been widely used as a signal on plant photochemical function. Global retrievals of solar-induced chlorophyll fluorescence (SIF) have become available over the recent years [20–23]. Recent studies have shown that SIF is a good proxy for vegetation photosynthesis or gross primary productivity (GPP) [21,24–28]. Under drought conditions, satellite-based SIF data have also been used to monitor large-scale vegetation status in Amazon forest [15], Midwest US [29], Russia [30], and Australia [31]. These studies show that SIF provides unique, perhaps the most direct, spatial information for early warning and accurate monitoring of appearing drought.

Southeast Asia has 2.1 million km² of forests, only accounting for 17% of the area of global tropical forests [32] but with 26% of the global tropical forest biomass carbon stock [33]. This implies that it has some of the highest carbon density regions on the planet compared to other tropical regions. As an important area of tropical vegetation, few studies have focused on the drought impacts on vegetation in Southeast Asia in comparison to a number of studies in the Amazon area [15,34] and African tropical ecosystems [16,35]. Furthermore, agriculture constitutes the largest sector in the economy of Southeast Asia, accounting for 40 percent GDP. However, agriculture in this region highly depends upon rainfall which occurs during the wet season. Since plant growth and carbon uptake are constrained to a large extent by drought [3], it is important and urgent to monitor and investigate the impacts of the widespread drought induced by the 2015/2016 El Niño event on land vegetation for agricultural planning and carbon budgets in this region. From Oceanic Nino Index (ONI), the 2015/2016 El Niño started at the end of 2014, peaked in late 2015, and ended in May 2016. It lasted 19 months and was 6 months longer than the 1997–1998 El Niño, the strongest El Niño on record [36]. However, direct evidence of the drought impacts during the 2015/2016 El Niño event on Southeast Asia vegetation is currently lacking.

In this study, we evaluated the degree of this drought over Southeast Asia by using multiple satellite-based dataset-conventional greenness-based VIs, newly available retrievals of SIF and meteorological data. In particular, we examined whether SIF can be an early indicator for large-scale vegetation health status under water stress in the tropical region.

2. Materials and Methods

2.1. Study Region

Southeast Asia is located between longitudes 92°E and 140°E and latitudes 10°S and 24°N. Two sub-areas were mainly focused (framed in Figure 1) in this paper according to the land cover types: the northwest region with high density of crops (8–18°N, 98–110°E) and the south region with high density of evergreen broadleaf forests (EBF) (5°S–5°N, 107–118°E). The Land Cover Type Yearly Climate Modeling Grid (CMG) product (MCD12C1) provided the dominant land cover types at 0.05° spatial resolution. We used MCD12C1 dataset in 2015 with University of Maryland (UMD) classification scheme. For the land cover dataset, it offered separate layers for each coverage type and the coverage percent values range from 0 to 100 for unique land cover types. The regions with less than 10% crop coverage and less than 70% EBF coverage were not considered in this paper.

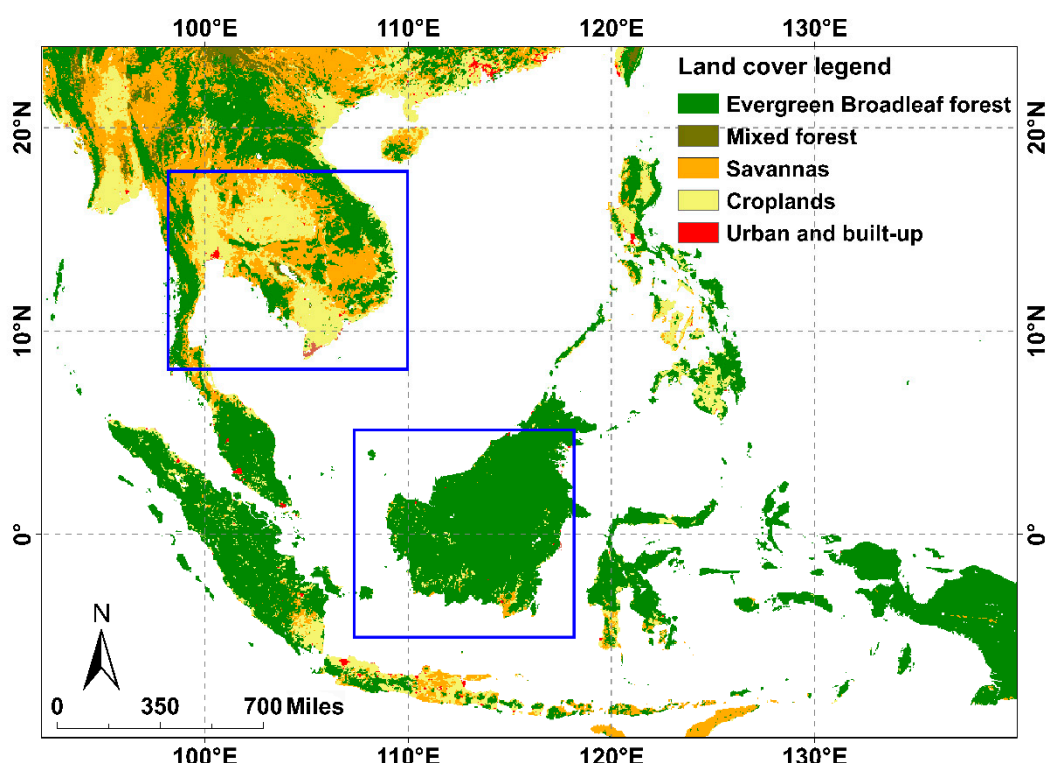


Figure 1. Land cover map of Southeast Asia, with the northwest region (8–18°N, 98–110°E) and the south region (5°S–5°N, 107–118°E) dominated by crops and evergreen broadleaf forest respectively.

2.2. Climate Dataset

Multiple climatic variables were employed to help interpret the temporal and spatial dynamics of SIF during the drought event. We utilized monthly mean temperature at 0.5° spatial resolution from the Climate Research Unit (CRU) dataset, which was based on monthly observational data, calculating from daily or sub-daily data [37]. The precipitation was taken from Tropical Rainfall Measuring Mission (TRMM) at 0.25° spatial resolution and daily temporal resolution from 2007 to 2016. TRMM data have been widely applied to explore the seasonal and interannual variations of precipitation in tropical continents. In terms of solar radiation, we used surface downscaling shortwave flux in all-day conditions at 1° spatial resolution over the period 2007–2016 from Clouds and the Earth's Radiant Energy System (CERES). To study the variability of aerosols, monthly mean of aerosol optical depth (AOD) from the Moderate resolution Imaging Spectroradiometer (MODIS) was used. AOD is the degree to which aerosols prevent absorbing and scattering light and can be used as an effective indicator of aerosol concentration [38].

Gravity Recovery and Climate Experiment (GRACE) observed monthly total water storage anomalies (TWS) in Earth's gravity field due to mass redistribution, which were caused mainly by the movement of water in a variety of surface and groundwater reservoirs [39]. We applied the mascon solutions from Centre for Space Research release 05 (CSR RL05) [40] from 2007 to 2016 to analyse the water content in the study area. The GRACE total water storage anomalies used in these mascon solutions were relative to the baseline average over January 2004 to December 2009 [40]. The Palmer Drought Severity Index (PDSI), an effective indicator of soil moisture in terms of precipitation and temperature [41], was utilized to illustrate the severity of various drought events [42]. The traditional PDSI used a set of empirical weighting factors derived from the average results from the US Great Plains. While the monthly self-calibrating PDSI (scPDSI) determined specific factors for each location separately, individually appropriate to that location [43]. Compared with PDSI data, scPDSI is a more suitable index to compare the spatio-temporal variability of soil moisture globally. The scPDSI data at 0.5° spatial resolution used in this study were derived from CRU climate dataset [44].

2.3. Satellite Vegetation Indices (VIs) and XCO₂ Data

Compared with NDVI, EVI reduced influences from the atmosphere and canopy background and improved sensitivity in high biomass areas to enhance the vegetation signal [16]. We used the 0.05° monthly EVI data (MOD13C2, V6), which contained quality assurance flags layers from 2007 to 2016. We only employed good quality EVI data (pixel reliability = 0) without contamination of clouds or aerosols in this study. Moreover, bidirectional reflectance distribution function (BRDF) correction for small biases was applied for EVI data.

We utilized the Greenhouse gases Observing SATellite (GOSAT) short-wave infrared Fourier transform spectrometer (FTS) data from April 2009 to December 2016, the v201 version of the L1B calibrated spectral radiance. We detrended the GOSAT XCO₂ data by correcting for the year-to-year average global XCO₂ trend. The Orbiting Carbon Observatory-2 (OCO-2) observed the CO₂ bands at wavelength in 1.61 and 2.06 μm and aimed to measure the column-averaged CO₂ dry-air mole fraction, XCO₂, to identify and characterize sources and sinks of CO₂ on regional scales [45]. O'Dell et al. [46] applied the Atmospheric CO₂ Observations from Space algorithm to retrieve the XCO₂. In addition, the OCO-2 SIF at 757 nm was a serendipitous but important supplementary by-product.

2.4. Satellite Chlorophyll Fluorescence Data

We used satellite SIF data retrievals from the Global Ozone Monitoring Experiment-2 (GOME-2) instrument on MetOp-A platform, which used channel 4 with the spectral resolution of 0.5 nm and near the wavelength of 740 nm far-red peak. The SIF at 740 nm was retrieved from a spectral range between 720 and 758 nm with an improved algorithm [21,22,47], which reduced the retrieval noise and sensitivity of the SIF retrieval to cloud contamination. Specifically, we applied the monthly gridded SIF product at 0.5° resolution from 2007 to 2016. The product has removed the data when the cloud fraction is greater than 0.5 for the cloud filtering. The GOME-2 instrument degraded significantly during its lifetime, particularly in the early stage of the record [48]. Therefore, we detrended SIF product to remove the degradation to allow focused analysis on interannual variability.

Chlorophyll fluorescence yield is a sensitive indicator for the photochemical and biochemical processes of photosynthesis [49]. The fluorescence yield of the canopy and the fraction of the canopy emission escaping to the atmosphere can be indicated by SIF yield (SIF_{yield}). SIF contained the amount of absorbed photosynthetically active radiation (APAR) and can be formulated as [24,29,30]:

$$SIF = APAR \times \varepsilon_f \times \Omega_c \quad (1)$$

$$SIF_{yield} = \frac{SIF}{APAR} \quad (2)$$

$$APAR = EVI \times Radiation \quad (3)$$

where ε_f is the actual fluorescence yield at the leaf level, and Ω_c is the probability of SIF photons escaping from the top of the canopy. SIF_{yield} is defined as the actual fluorescence yield at the top of the canopy. SIF_{yield}, which is related to leaf biochemistry and canopy structure, removes the impact of APAR on SIF. This variable can indicate the dynamic process of SIF and photosynthetic efficiency of plants when the drought occurs [29]. Since the amount of incoming photosynthetically active radiation is proportional to the total downwelling shortwave radiation, the products of shortwave radiation and EVI were used to calculate APAR [50].

2.5. Analysis

The resolution of different data sets used in this study varied at the spatial and temporal scale. In order to minimize potential differences due to the mismatch in spatial and temporal resolution, we aggregated all the variables to $0.5^\circ \times 0.5^\circ$ and monthly mean to maintain the consistency with GOME-2 SIF data.

To obtain signals related to the drought stress, the spatial distribution of normalized anomalies of SIF, SIF_{yield}, EVI, temperature, precipitation, and radiation were computed at the pixel level. The anomaly in a pixel (i, j) for the drought year 2015 and 2016 was calculated as a departure from that averaged of the period 2007–2014 and normalized by the standard deviation (std):

$$x_{2015/2016 \text{ anomaly}}((i, j)) = \frac{x_{2015/2016}(i, j) - \text{mean}(x_{2007-2014}(i, j))}{\text{std}(x_{2007-2014}(i, j))} \quad (4)$$

The anomalies indicated the departure from their relevant multiyear mean for each month. The GOSAT XCO₂ data were only available from 2009 to 2016; thus anomalies were calculated as deviations from the average of the period 2009–2014.

3. Results

3.1. The 2015/16 Drought

Firstly, the temperature and precipitation anomalies were analyzed in the two sub-areas (regions framed in Figure 1). Compared to the annual mean precipitation during 2007 to 2014 (Figure 2a), the crop area experienced continuous severe precipitation deficits in 2015 (with minimum anomaly -148.71 mm in October) and recovered in 2016. Moreover, substantially warmer temperatures (with maximum anomaly 2.04°C in April of 2016) during the 2015/16 El Niño event made the drought unique and extreme (Figure 2a). The values of scPDSI were below 0 from the end of 2014–2016 (Figure 2b), which corresponded well to the period of El Niño event. In addition, this extreme drought can also be detected from the persistent negative values of TWS (Figure 2b). Higher temperature and less precipitation led to the sustained deficits of TWS and much lower scPDSI values in the crop region. The values of scPDSI in several extreme dry months were less than -2 , reaching moderate drought level (Figure 2b). In EBF area, the precipitation was slightly below the average in late 2015 and early 2016 (with minimum anomaly -85.82 mm in December of 2015) and the temperature increased continuously (with maximum anomaly 1.13°C in April of 2016) (Figure 2c). Increased temperature and decreased precipitation affected groundwater conditions in this area, leading to a substantial reduction of TWS during the drought. The values of scPDSI were less than -1 , which indicated the mild drought level. And the low scPDSI lasted up to 7 months (from July in 2015 to January in 2016) (Figure 2d). Owing to the increase of precipitation in the EBF area, the scPDSI gradually became positive in 2016, indicating the recovery of regional drought conditions.

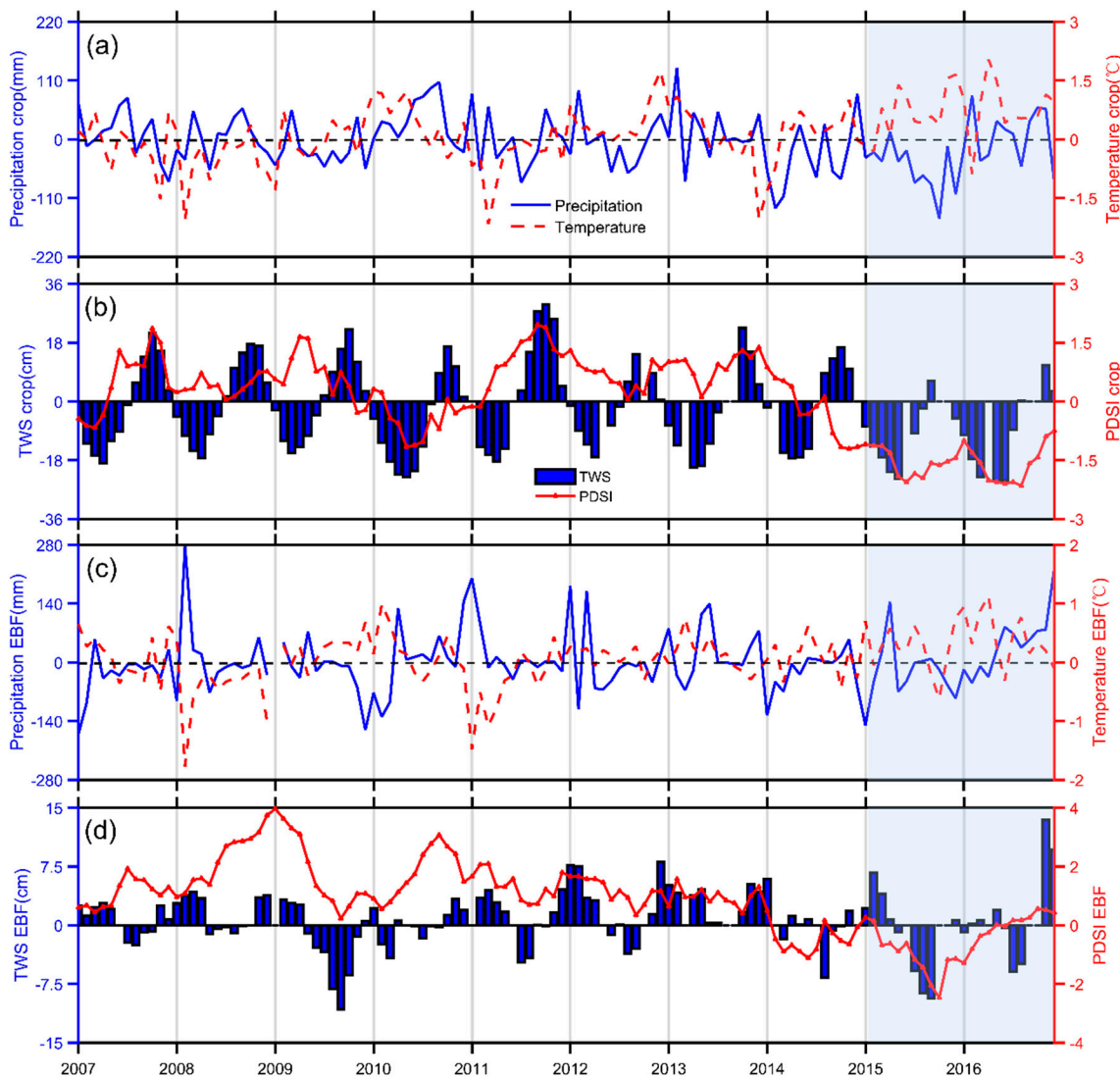


Figure 2. Monthly anomalies of temperature, precipitation, TWS and scPDSI in croplands (**a,b**) and in evergreen broadleaf forest area (**c,d**) from January 2007 to December 2016. The shaded area showed the drought years.

Spatially, temperature anomalies in 2015/16 (Figure 3a,b) exceeded two standard deviations relative to the multiyear mean from 2007 to 2014 over the most of Southeast Asia. Large increases of temperature existed in 2016 and the anomalies were larger than three standard deviations from the multiyear mean over the EBF area. Significant positive anomalies in radiation, with larger than three standard deviations in 2015, were observed over cropland area in 2015 and 2016 (Figure 3e,f). In EBF areas, radiation dropped dramatically in 2015 because of the fire which happened in Indonesia from September to October in 2015 [6] but significantly increased in 2016 which agreed well with the changes of temperature. In addition, the two studied areas experienced water deficits in 2015 and the precipitation anomalies in cropland area were smaller than 1.5 standard deviations relative to the multi-year mean. Precipitation recovered in 2016 in most parts of EBF area. According to the drought index, scPDSI showed negative values in cropland area in 2015 and 2016, while the values of scPDSI became positive in some parts of EBF area in 2016 (Figure 3g,h). The two sub-areas were greatly affected by the severe drought induced by the strong El Niño event during 2015 and 2016. Therefore, it is important to investigate the drought impacts on vegetation productivity of crop and forest in Southeast Asia.

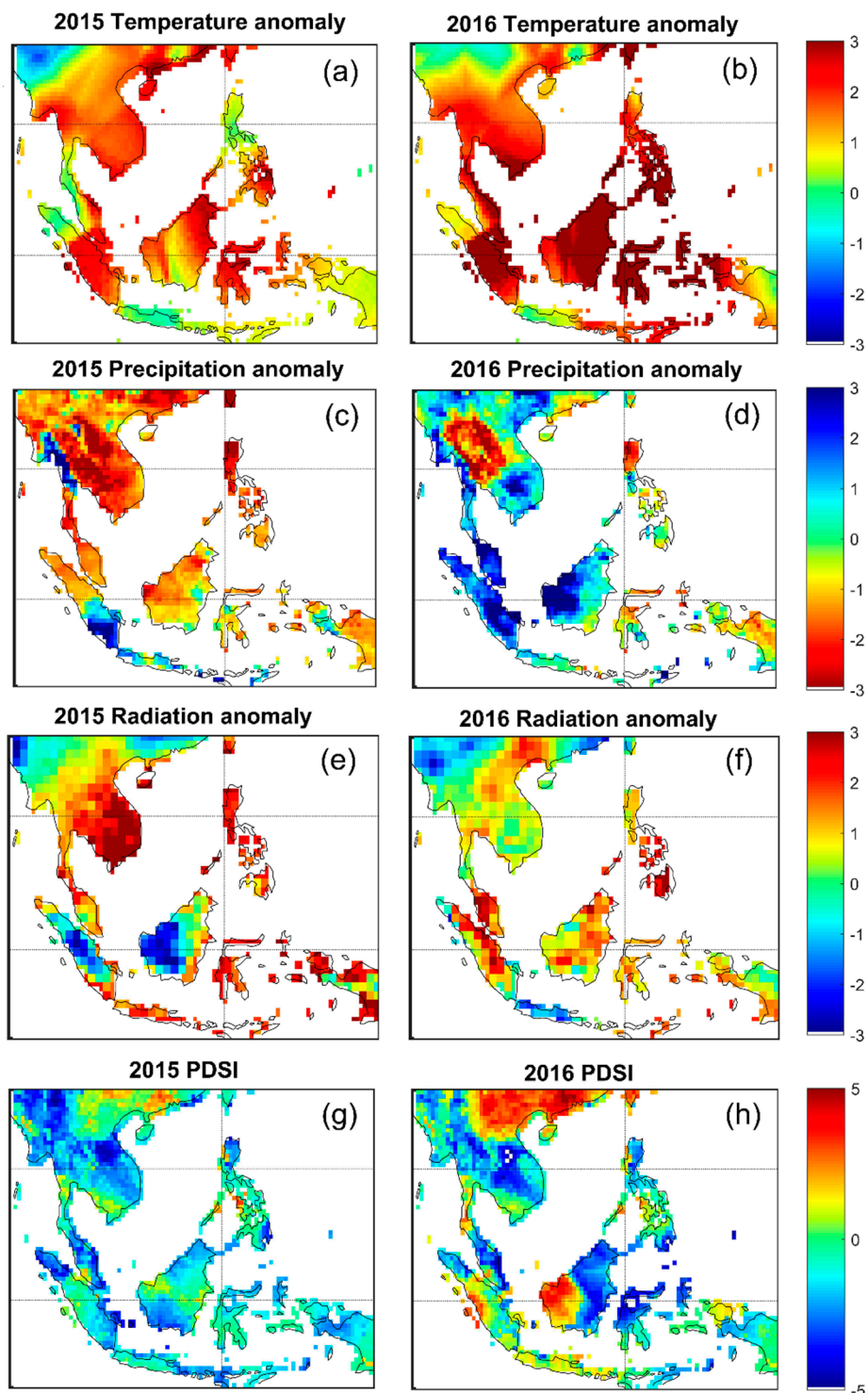


Figure 3. The spatial distribution of normalized anomalies of (a,b) temperature, (c,d) precipitation, (e,f) radiation and (g,h) scPDSI in 2015 and 2016 relative to the means over the period 2007–2014 in Southeast Asia.

3.2. Response of Vegetation to Drought

In this part, how vegetation productivity responded to this drought event were investigated in the crop and forest regions. Figure 4 showed the spatial distributions of normalized anomalies of EVI, SIF and SIF_{yield} in 2015 and 2016. For cropland, the spatial patterns presented by EVI anomalies showed an increase compared to the multiyear mean in most of cropland both in 2015 and 2016.

SIF had positive anomalies during the early stage of the drought, but turned to negative pattern at the end of the drought. For the SIF_{yield}, substantial SIF_{yield} reduced throughout cropland in both years, with 41.81% and 38.42% of severe losses ($<1\sigma$) in 2015 and 2016, respectively (Figure 4). For EBF region, it had very similar results with that from the cropland. The satellite observations of SIF_{yield} showed a response to this drought with a reduction of approximately 60.54% in 2016. However, the EVI and SIF showed slight increases in 2016, which was not able to capture the negative response to the drought.

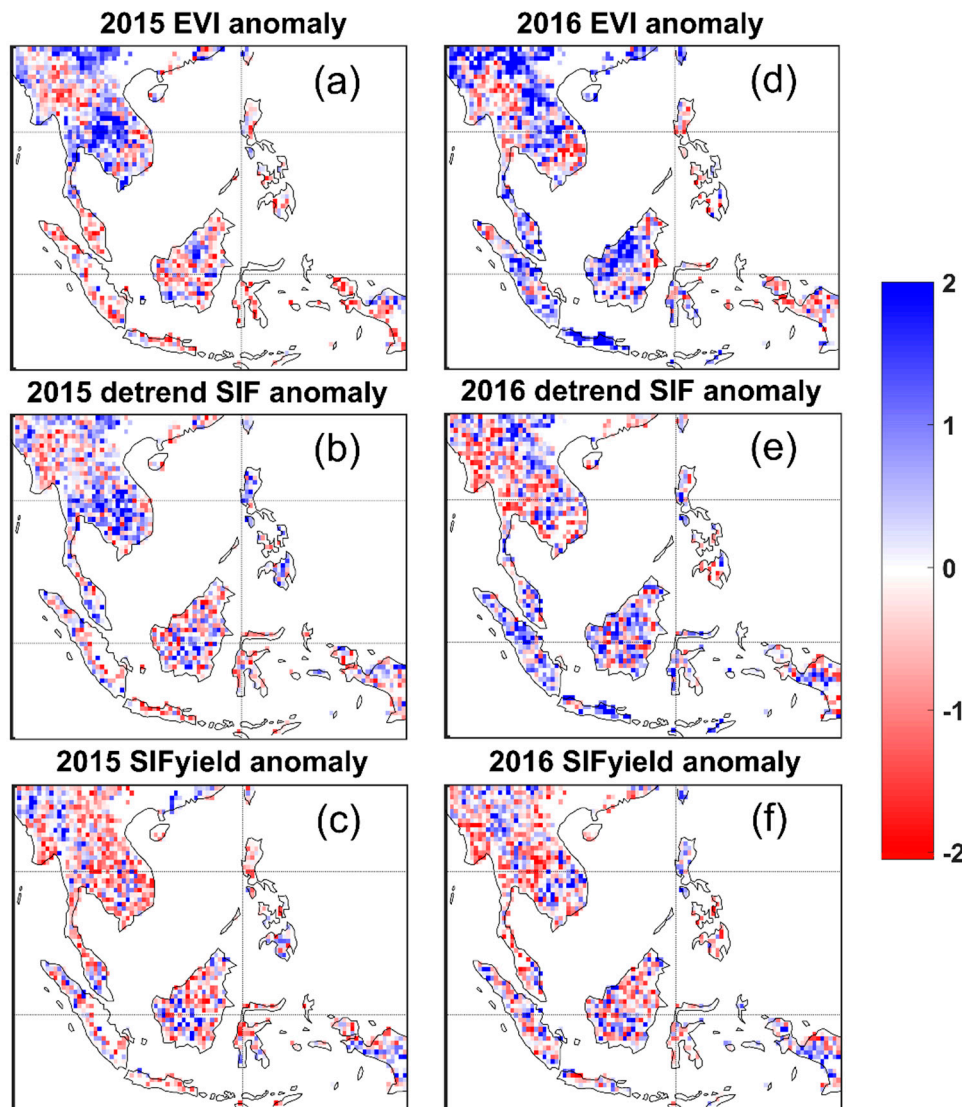


Figure 4. The spatial distribution of normalized anomalies of (a,d) EVI, (b,e) SIF, (c,f) SIF_{yield} in 2015 (left column) and 2016 (right column) relative to the means over the period 2007–2014 in Southeast Asia.

Figure 5 showed the probability density of the spatial standard anomalies for the drought years. In cropland areas, the largest probability density of cropland precipitation in 2015 shifted left dramatically and it was slightly less than 0 in 2016. Meanwhile, the SIF_{yield} shifted left obviously for both years, which indicated that negative SIF_{yield} anomalies were existed in most of the study area. The largest probability density of SIF shifted left slightly in 2015 and significantly in 2016. However, the largest probability density of cropland EVI did not indicate any drought signal in 2015 and 2016. For the EBF area, the changes in maximum probability density of these factor anomalies were broadly similar, moving slightly left in 2015 and recovering in 2016, which indicated moderate drought

condition in 2015. Overall, the spatial analysis demonstrated that satellite SIF_{yield} available from current instruments had the potential to describe the impacts of drought on the vegetation growth.

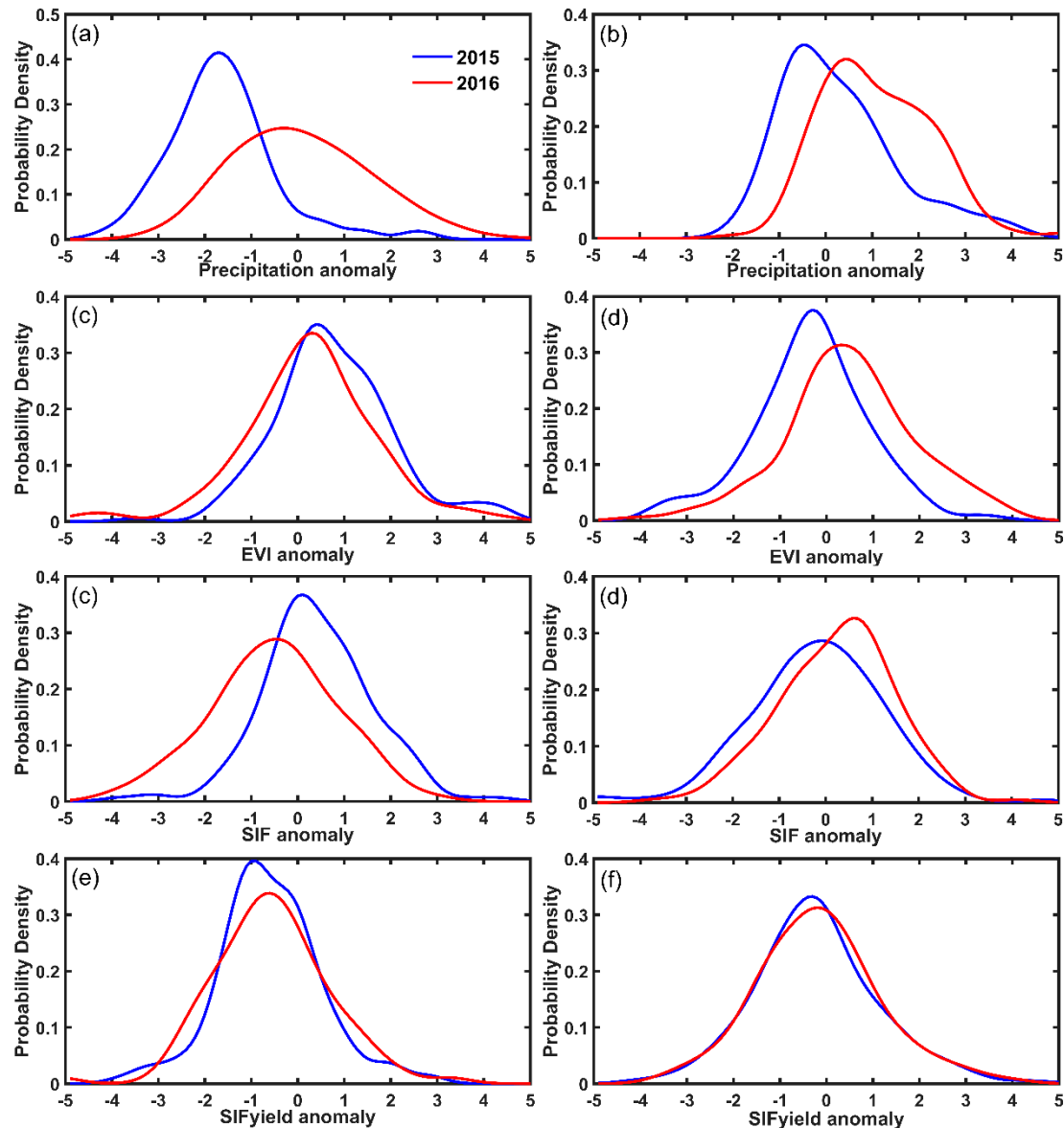


Figure 5. The probability density of normalized anomalies of (a,b) Precipitation, (c,d) EVI, (e,f) SIF, (g,h) SIF_{yield} in 2015 and 2016 relative to that of over the period 2007–2014 in croplands (left column) and evergreen broadleaf forest area (right column).

The strong El Niño during 2015 and 2016 peaked in late 2015, and ended in May 2016 [36]. We further examined the seasonal cycles of the vegetation and climate variables (precipitation, EVI, SIF, and SIF_{yield}) over drought period (from May 2015 to April 2016) in the two sub-areas (Figure 6). For the cropland, the values of EVI were higher than the multiyear mean for most months during the drought period (Figure 6c). SIF had larger reductions than EVI during the early stages of the drought (May to August 2015). As a consequence, SIF had more potential than EVI to monitor the spatial patterns when drought occurred in cropland areas. The SIF_{yield} was much smaller than the multiyear mean for most of the dry months (Figure 6g) and had a similar trend in precipitation (Figure 6a). During the drought period, SIF was affected by higher radiation which can offset the negative impacts of water stress, leading to the smaller decrease of SIF compared with the large negative anomalies of SIF_{yield}.

Therefore, SIF_{yield} can be a better indicator to describe the developments of drought impacts of water stress on crop growth.

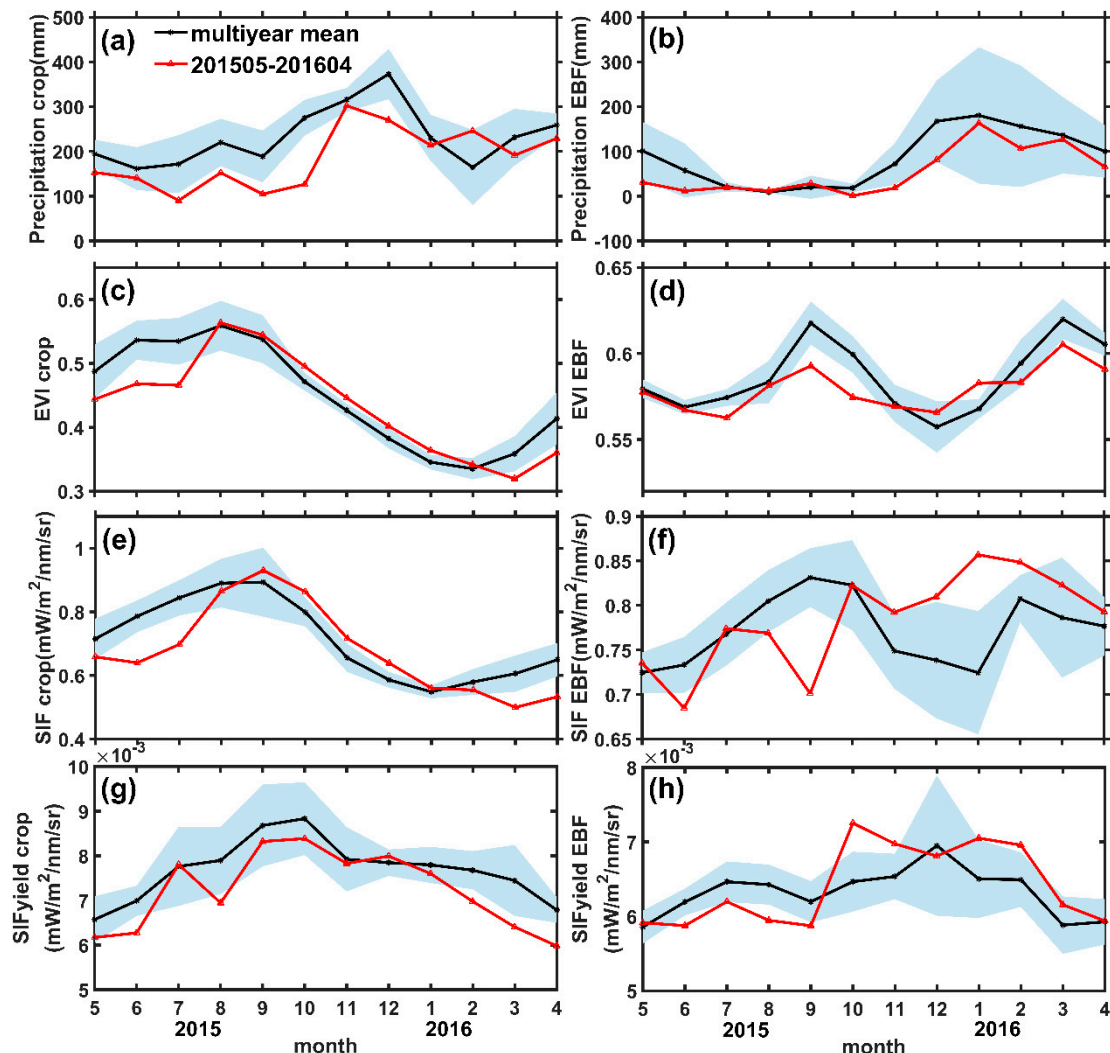


Figure 6. The monthly averages of (a,b) precipitation, (c,d) EVI, (e,f) SIF, (g,h) SIF_{yield} for the croplands (left column) and for the evergreen broadleaf forest area (right column) during the drought period (from May 2015 to April 2016) in Southeast Asia. The shaded area showed uncertainties of the multiyear mean from 2007 to 2014.

The drought condition in the EBF region was moderate during the El Niño event (Figure 6b). The decline of EVI, SIF, SIF_{yield} in EBF regions were similar during the El Niño peak time. However, a sudden increase of SIF_{yield} appeared from September to October in 2015. The substantial decrease of solar radiation in EBF area was in September 2015 (Figure 3e), which coincided with the highest monthly aerosol optical depth (Figure 7) caused by fire in September in Indonesia [6]. Consequently, SIF_{yield} increased in October and November because of the fire in EBF area. But for the other months, SIF_{yield} was less than multiyear mean in late 2015. Both regions exhibited larger reduction of SIF_{yield} than that of SIF and EVI during the drought peak time. The SIF_{yield} quickly responded when the drought began, and anomalies of SIF_{yield} became larger as the drought aggravated. The analyses for the crop and EBF regions indicated that the SIF_{yield} not only described the spatial patterns of the drought event but also captured the temporal dynamics of their impacts on effective fluorescence yield.

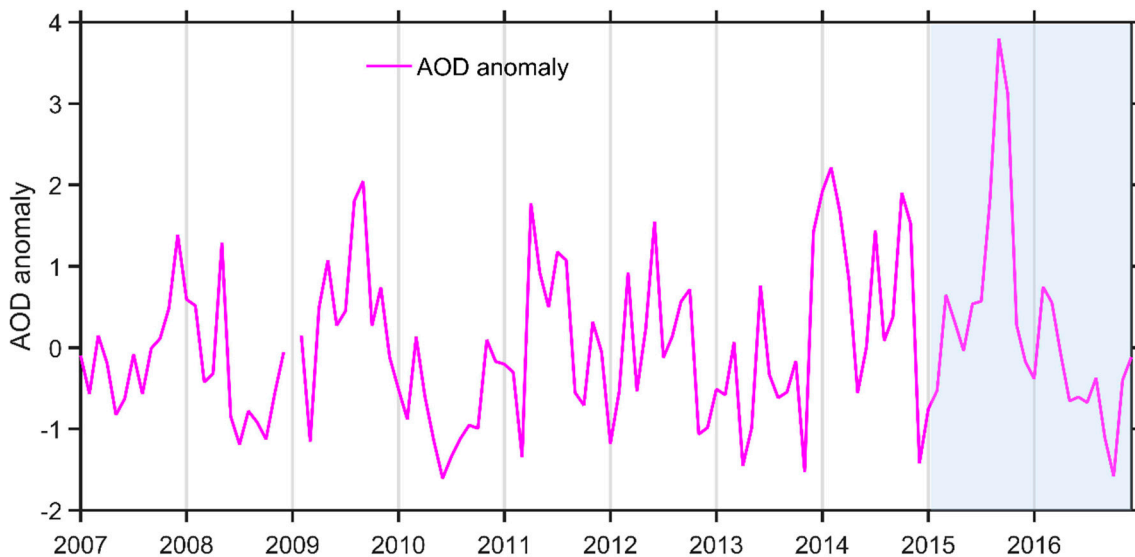


Figure 7. Normalized anomalies of aerosol optical depth (AOD) for Southeast Asia from 2007 to 2016. The shaded area showed the drought years.

3.3. Implications on the Regional Carbon Cycle

The variations in atmospheric CO₂ are mostly due to fluctuating carbon uptake by terrestrial ecosystems [51]. The GOSAT detrended XCO₂ average value was used to investigate the changes of atmospheric CO₂ during this strong El Niño event in Southeast Asia. The whole area of Southeast Asia was averaged owing to the coarse spatial resolution of XCO₂ data. The XCO₂ showed a consistent negative correlation with SIF and EVI (Figure 8)

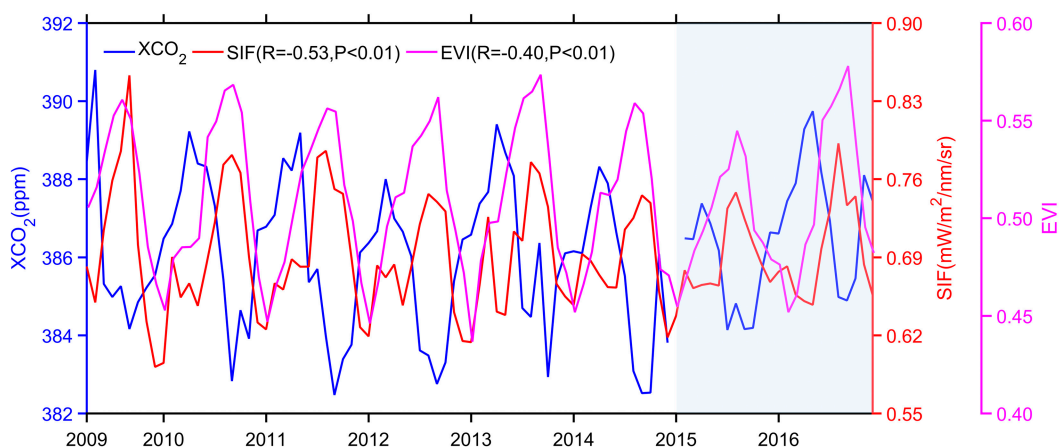


Figure 8. Monthly average of XCO₂, EVI and SIF for the Southeast Asia from April 2009 to 2016. The shaded area showed the drought years.

The correlation coefficient between SIF and XCO₂ ($R = -0.53, p < 0.01$) was more significant than that between EVI and XCO₂ ($R = -0.40, p < 0.01$). As mentioned before, this El Niño peaked in late 2015 and ended in May 2016. SIF showed better capability to capture the response of vegetation to the drought. Figure 8 displayed that in 2016 the CO₂ emission rose drastically from March along with SIF and EVI went down to the lowest value, which was 5 months behind the fire event. During this period, SIF was highly correlated to XCO₂, much more relevant than EVI.

OCO-2 is the first NASA satellite designed to measure and characterize CO₂. The relationship between the OCO-2 SIF and XCO₂ was also investigated based on the OCO-2 products. The average values of OCO-2 XCO₂ and SIF from 2015 to 2017 were shown in Figure 9. SIF fell with the rising XCO₂

during this period, indicating that vegetation status was relevant with CO₂ concentration. OCO-2 XCO₂ and SIF products had a strong negative correlation ($R = -0.59, p < 0.01$), which could show the high potential of OCO-2 data for the drought research in the future.

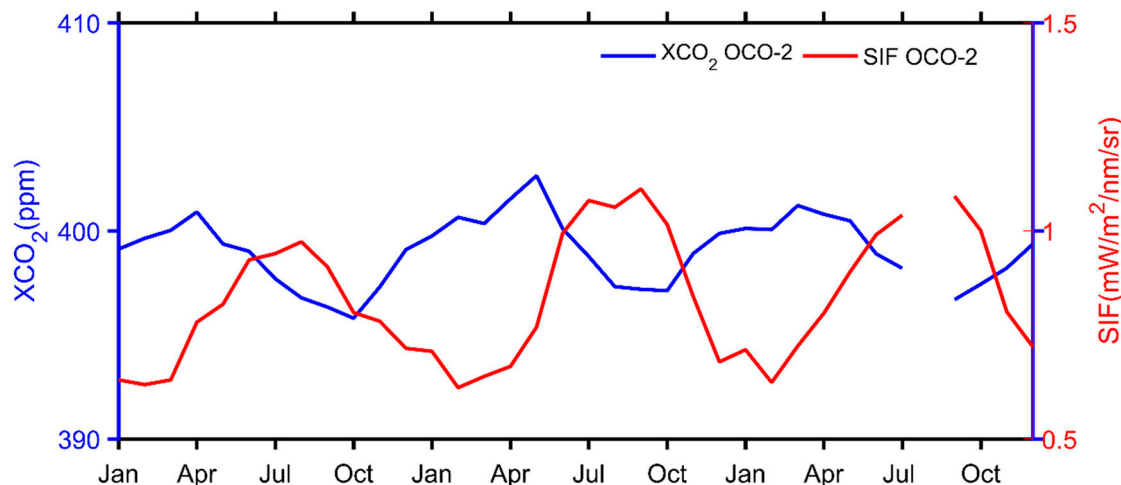


Figure 9. Monthly average of OCO-2 XCO₂, SIF for the Southeast Asia from 2015 to 2017.

The net fluxes of production and consumption processes from both natural and anthropogenic sources can be reflected by dynamics of column CO₂. And our results confirmed that SIF, as a proxy for vegetation status, can indirectly reflect the regional CO₂ variations, especially when the water deficit occurred. Water deficit usually results in the closure of stomata, which then reduces the absorption of CO₂ and makes photosynthesis slow down [52]. Thus, a strong carbon emission occurred along with the decreased SIF in Southeast Asia from the end of 2015 to mid-2016 because of the water deficit. Atmospheric CO₂ variability is driven by a wide range of processes, such as temperature change, drought/flooding, fire emissions, and land use changes, which all play significant roles in changing the carbon land sink at global and regional scales [53]. Using satellite SIF observations, we can better understand the underlying processes and improve the performance of biochemical models, which still contained many uncertainties for the simulations of carbon cycle [54].

4. Conclusions and Discussion

In this paper, based on the satellite EVI and SIF products along with other climate and vegetation datasets, we examined the impacts of drought on the vegetation photosynthesis for crops and forests in Southeast Asia during the 2015/16 El Niño event. We found that satellite SIF observations were more sensitive than traditional VIs to monitor water stress for both evergreen broadleaf forest and croplands in Southeast Asia. Therefore, the space-borne SIF can be used as an effective indicator to predict the response of vegetation to water and heat stresses in the tropical region. Previous studies have reported that the higher solar radiation motivates leaf flush and leaf expansion in forests [35,55,56]. Leaf area index could be first enhanced because of the increased solar radiation, and then EVI. As a result, two regions in Southeast Asia showed green up when the drought happened according to the increases of EVI anomalies, which was related to the higher radiation (Figures 3–5). Similarly, SIF cannot characterize drought well compared to SIF_{yield} in the late 2015 in both areas because of high radiation, but it still showed higher sensitivity to drought than EVI. SIF showed more negative anomalies than EVI (Figure 4) because SIF was directly linked to the vegetation functioning, indicating that SIF can potentially be used as proxy for monitoring vegetation droughts with different onset mechanisms. Moreover, the impacts of drought on SIF became more pronounced when the effect of radiation was removed (Figures 5 and 6). This phenomenon was observed for both vegetation types. Previous studies have demonstrated that the water stress altered the LAI during the drought [30]. As we know,

LAI is an important canopy structure parameter and has a direct impact on the fraction of absorbed photosynthetic active radiation (fPAR). Qiu et al. [57] used a generalized radiative transfer model within the canopy to investigate the relationship between fPAR and LAI, and the results demonstrated that fPAR increased with higher LAI. Therefore, the altered fPAR and APAR during the drought may have strong impacts on radiative transfer process of SIF and the probability that SIF photons escaping from the canopy. And our results also confirmed that the drought had more pronounced impacts on SIF_{yield} than SIF and EVI because of elimination of the effects of the solar radiation variations in SIF_{yield} . The effects of vegetation structural variables were eliminated, then important information on drought events could be provided by SIF_{yield} . Changes on vegetation greenness and chlorophyll content may not rapidly reflect the information about vegetation status under drought, but variations on the production of fluorescence have rapid responses to water stress [26,29,30,58]. Therefore, SIF_{yield} is the suitable factor to detect the changes of vegetation function during the drought period in the study areas.

The strong 2015/2016 El Niño provided an opportunity to investigate the response of tropical terrestrial ecosystems to extreme climatic event [36]. Previous studies focused on the drought impacts of the 2015/2016 El Niño events in the tropics [58,59] and figured out the mechanisms affected canopy photosynthesis. More studies demonstrated that the GPP decreased due to the extreme drought in the tropics [36,60]. The enhanced PAR did not increase GPP in Amazon during the 2015/2016 drought [61]. Field experiments at the Amazon KM83 site convinced that strong radiation resulted in increased leaf temperature, which reduced canopy photosynthesis [60]. Koren et al. [62] applied SIF to quantify the impact of the 2015/2016 El Niño drought in Amazon and found that SIF was strongly inhibited over areas with anomalously decreased soil moisture and high temperatures.

The strong El Niño event also had substantial impacts on the variations of atmospheric CO_2 at global and regional scales. Previous studies [36,51,63] have demonstrated that the terrestrial tropics dominated the interannual variability of the global carbon cycle. Based on the simulations from global terrestrial biosphere models, Luo et al. [64] showed that global photosynthesis decreased in 2015 and the decrease in GPP led to 60% of the net ecosystem productivity (NEP) reduction. Since El Niño affected mainly on tropical ecosystems, the growth rate of CO_2 in 2015/2016 was higher than the average of previous decade [58]. When the 2015/2016 El Niño events and the fire in Indonesia occurred, tropical Asia experienced severe losses of SIF and GPP, along with increased carbon release [36]. Our results demonstrated that the XCO_2 had a strong negative correlation with SIF, indicating the carbon emission in Southeast Asia during 2015 and 2016 (Figure 9). The satellite SIF data can indirectly reflect the regional CO_2 variations, especially when the vegetation experienced environmental stresses. Water stress usually results in the stomata closure for plant, then makes photosynthesis slow down and reduces the absorption of atmospheric CO_2 [52]. Therefore, satellite SIF can be used to estimate the variations of atmospheric CO_2 growth rate during the extreme climate events.

In summary, we found that space-borne SIF observations had great potential for monitoring the spatial and temporal response of plant growth to drought in general, with El Niño event as an example. The EVI was not able to capture the negative response of the vegetation to drought. However, satellite SIF data had more pronounced responses to extreme events than EVI when the drought occurred. Moreover, compared with SIF, SIF_{yield} can provide more accurate information about vegetation conditions during the drought period as it removed the effects of APAR. This study indicated that satellite-based SIF reasonably characterized the spatial and temporal dynamics of drought development in crop and forest regions in Southeast Asia. Responses of vegetation photosynthesis and greenness decoupled in this extreme drought, indicating that satellite-based SIF products would be a better choice for the response of vegetation to extreme climate events induced by the strong El Niño events in the future.

Author Contributions: Conceptualization, Y.Z.; Data curation, X.Q.; Formal analysis, X.Q. and B.Q.; Investigation, X.Q.; Methodology, B.Q. and Y.Z.; Software, X.Q.; Supervision, Y.Z.; Writing—original draft, X.Q.; Writing—review & editing, B.Q. and Y.Z.

Funding: This research is financially supported by the International Cooperation and Exchange Programs between NSFC and DFG (41761134082) and General Program of National Science Foundation of China (41671421), Natural Science Foundation of China (41705056) and the Natural Science Foundation of Jiangsu Province (BK20170638).

Acknowledgments: All the MODIS data (Land Cover product, AOD, EVI) were generated from MODIS LP DAAC archive. Temperature, scPDSI were obtained from CRU, and precipitation from TRMM. Radiation used in this study was downloaded from CERES. GRACE RL05 mascon data were received from Center for Space Research at http://www2.csr.utexas.edu/grace/RL05_mascons. We want to thank Philip Köhler for providing the GOME-2 SIF data which used a linear method through <ftp://fluo.gps.caltech.edu/data/Philip/GOME-2/>. We also acknowledge the OCO-2 team for making XCO₂ and SIF data available, which were obtained from <http://disc.gsfc.nasa.gov/OCO-2>. GOSAT data was granted through <http://www.esa-ghg-cci.org>. We thank Sophia Walther and Lian Song for providing suggestions for analysing these data.

Conflicts of Interest: The authors declare no conflict of interest.

References

1. Detmers, R.; Hasekamp, O.; Aben, I.; Houweling, S.; Van Leeuwen, T.; Butz, A.; Landgraf, J.; Köhler, P.; Guanter, L.; Poulter, B. Anomalous carbon uptake in Australia as seen by GOSAT. *Geophys. Res. Lett.* **2015**, *42*, 8177–8184. [[CrossRef](#)]
2. Page, S.E.; Siegert, F.; Rieley, J.O.; Boehm, H.-D.V.; Jaya, A.; Limin, S. The amount of carbon released from peat and forest fires in Indonesia during 1997. *Nature* **2002**, *420*, 61. [[CrossRef](#)]
3. Reichstein, M.; Bahn, M.; Ciais, P.; Frank, D.; Mahecha, M.D.; Seneviratne, S.I.; Zscheischler, J.; Beer, C.; Buchmann, N.; Frank, D.C. Climate extremes and the carbon cycle. *Nature* **2013**, *500*, 287. [[CrossRef](#)] [[PubMed](#)]
4. Glikson, A. Cenozoic mean greenhouse gases and temperature changes with reference to the Anthropocene. *Glob. Chang. Biol.* **2016**, *22*, 3843–3858. [[CrossRef](#)]
5. Blunden, J.; Arndt, D.S. State of the climate in 2015. *Bull. Am. Meteorol. Soc.* **2016**, *97*, S275. [[CrossRef](#)]
6. Huijnen, V.; Wooster, M.J.; Kaiser, J.W.; Gaveau, D.L.; Flemming, J.; Parrington, M.; Inness, A.; Murdiyarso, D.; Main, B.; van Weele, M. Fire carbon emissions over maritime southeast Asia in 2015 largest since 1997. *Sci. Rep.* **2016**, *6*, 26886. [[CrossRef](#)]
7. Jiménez-Muñoz, J.C.; Mattar, C.; Barichivich, J.; Santamaría-Artigas, A.; Takahashi, K.; Malhi, Y.; Sobrino, J.A.; Van Der Schrier, G. Record-breaking warming and extreme drought in the Amazon rainforest during the course of El Niño 2015–2016. *Sci. Rep.* **2016**, *6*, 33130. [[CrossRef](#)] [[PubMed](#)]
8. Wang, Y.; Xie, Y.; Dong, W.; Ming, Y.; Wang, J.; Shen, L. Adverse effects of increasing drought on air quality via natural processes. *Atmos. Chem. Phys.* **2017**, *17*, 12827–12843. [[CrossRef](#)]
9. Van Der Schrier, G.; Klein Tank, A.M.; Van Den Besselaar, E.J.; Swarinoto, Y. Observed trends and variability in climate indices relevant for crop yields in Southeast Asia. *J. Clim.* **2016**, *29*, 2651–2669.
10. Peng, J.; Dadson, S.; Leng, G.; Duan, Z.; Jagdhuber, T.; Guo, W.; Ludwig, R. The impact of the Madden-Julian Oscillation on hydrological extremes. *J. Hydrol.* **2019**, *571*, 142–149. [[CrossRef](#)]
11. Mu, Q.; Zhao, M.; Kimball, J.S.; McDowell, N.G.; Running, S.W. A remotely sensed global terrestrial drought severity index. *Bull. Am. Meteorol. Soc.* **2013**, *94*, 83–98. [[CrossRef](#)]
12. Tucker, C.J.; Choudhury, B.J. Satellite remote sensing of drought conditions. *Remote Sens. Environ.* **1987**, *23*, 243–251. [[CrossRef](#)]
13. Gu, Y.; Brown, J.F.; Verdin, J.P.; Wardlow, B. A five-year analysis of MODIS NDVI and NDWI for grassland drought assessment over the central Great Plains of the United States. *Geophys. Res. Lett.* **2007**, *34*, L06407. [[CrossRef](#)]
14. Huete, A.; Didan, K.; Miura, T.; Rodriguez, E.P.; Gao, X.; Ferreira, L.G. Overview of the radiometric and biophysical performance of the MODIS vegetation indices. *Remote Sens. Environ.* **2002**, *83*, 195–213. [[CrossRef](#)]
15. Lee, J.-E.; Frankenberger, C.; van der Tol, C.; Berry, J.A.; Guanter, L.; Boyce, C.K.; Fisher, J.B.; Morrow, E.; Worden, J.R.; Asefi, S. Forest productivity and water stress in Amazonia: Observations from GOSAT chlorophyll fluorescence. *Proc. R. Soc. Biol. Sci.* **2013**, *280*, 20130171. [[CrossRef](#)] [[PubMed](#)]
16. Zhou, L.; Tian, Y.; Myneni, R.B.; Ciais, P.; Saatchi, S.; Liu, Y.Y.; Piao, S.; Chen, H.; Vermote, E.F.; Song, C. Widespread decline of Congo rainforest greenness in the past decade. *Nature* **2014**, *509*, 86. [[CrossRef](#)]

17. Asner, G.P.; Alencar, A. Drought impacts on the Amazon forest: The remote sensing perspective. *New Phytol.* **2010**, *187*, 569–578. [[CrossRef](#)]
18. Daumard, F.; Champagne, S.; Fournier, A.; Goulas, Y.; Ounis, A.; Hanocq, J.-F.; Moya, I. A field platform for continuous measurement of canopy fluorescence. *IEEE Trans. Geosci. Remote Sens.* **2010**, *48*, 3358–3368. [[CrossRef](#)]
19. Zarco-Tejada, P.J.; Miller, J.R.; Mohammed, G.H.; Noland, T.L.; Sampson, P.H. Chlorophyll fluorescence effects on vegetation apparent reflectance: II. Laboratory and airborne canopy-level measurements with hyperspectral data. *Remote Sens. Environ.* **2000**, *74*, 596–608. [[CrossRef](#)]
20. Frankenberg, C.; Fisher, J.B.; Worden, J.; Badgley, G.; Saatchi, S.S.; Lee, J.E.; Toon, G.C.; Butz, A.; Jung, M.; Kuze, A. New global observations of the terrestrial carbon cycle from GOSAT: Patterns of plant fluorescence with gross primary productivity. *Geophys. Res. Lett.* **2011**, *38*, L17706. [[CrossRef](#)]
21. Guanter, L.; Rossini, M.; Colombo, R.; Meroni, M.; Frankenberg, C.; Lee, J.-E.; Joiner, J. Using field spectroscopy to assess the potential of statistical approaches for the retrieval of sun-induced chlorophyll fluorescence from ground and space. *Remote Sens. Environ.* **2013**, *133*, 52–61. [[CrossRef](#)]
22. Joiner, J.; Guanter, L.; Lindstrom, R.; Voigt, M.; Vasilkov, A.; Middleton, E.; Huemmrich, K.; Yoshida, Y.; Frankenberg, C. Global monitoring of terrestrial chlorophyll fluorescence from moderate-spectral-resolution near-infrared satellite measurements: Methodology, simulations, and application to GOME-2. *Atmos. Meas. Tech.* **2013**, *6*, 2803–2823. [[CrossRef](#)]
23. Joiner, J.; Yoshida, Y.; Vasilkov, A.; Middleton, E. First observations of global and seasonal terrestrial chlorophyll fluorescence from space. *Biogeosciences* **2011**, *8*, 637–651. [[CrossRef](#)]
24. Guanter, L.; Zhang, Y.; Jung, M.; Joiner, J.; Voigt, M.; Berry, J.A.; Frankenberg, C.; Huete, A.R.; Zarco-Tejada, P.; Lee, J.-E. Global and time-resolved monitoring of crop photosynthesis with chlorophyll fluorescence. *Proc. Natl. Acad. Sci. USA* **2014**, *111*, E1327–E1333. [[CrossRef](#)]
25. Zhang, Y.; Guanter, L.; Berry, J.A.; van der Tol, C.; Yang, X.; Tang, J.; Zhang, F. Model-based analysis of the relationship between sun-induced chlorophyll fluorescence and gross primary production for remote sensing applications. *Remote Sens. Environ.* **2016**, *187*, 145–155. [[CrossRef](#)]
26. Song, L.; Guanter, L.; Guan, K.; You, L.; Huete, A.; Ju, W.; Zhang, Y. Satellite sun-induced chlorophyll fluorescence detects early response of winter wheat to heat stress in the Indian Indo-Gangetic Plains. *Glob. Chang. Biol.* **2018**, *24*, 4023–4037. [[CrossRef](#)]
27. Shan, N.; Ju, W.; Migliavacca, M.; Martini, D.; Guanter, L.; Chen, J.; Goulas, Y.; Zhang, Y. Modeling canopy conductance and transpiration from solar-induced chlorophyll fluorescence. *Agric. For. Meteorol.* **2019**, *268*, 189–201. [[CrossRef](#)]
28. Qiu, B.; Li, W.; Wang, X.; Shang, L.; Song, C.; Guo, W.; Zhang, Y. Satellite-observed solar-induced chlorophyll fluorescence reveals higher sensitivity of alpine ecosystems to snow cover on the Tibetan Plateau. *Agric. For. Meteorol.* **2019**, *271*, 126–134. [[CrossRef](#)]
29. Sun, Y.; Fu, R.; Dickinson, R.; Joiner, J.; Frankenberg, C.; Gu, L.; Xia, Y.; Fernando, N. Drought onset mechanisms revealed by satellite solar-induced chlorophyll fluorescence: Insights from two contrasting extreme events. *J. Geophys. Res. Biogeosci.* **2015**, *120*, 2427–2440. [[CrossRef](#)]
30. Yoshida, Y.; Joiner, J.; Tucker, C.; Berry, J.; Lee, J.-E.; Walker, G.; Reichle, R.; Koster, R.; Lyapustin, A.; Wang, Y. The 2010 Russian drought impact on satellite measurements of solar-induced chlorophyll fluorescence: Insights from modeling and comparisons with parameters derived from satellite reflectances. *Remote Sens. Environ.* **2015**, *166*, 163–177. [[CrossRef](#)]
31. Zhang, L.; Qiao, N.; Huang, C.; Wang, S. Monitoring Drought Effects on Vegetation Productivity Using Satellite Solar-Induced Chlorophyll Fluorescence. *Remote Sens.* **2019**, *11*, 378. [[CrossRef](#)]
32. Grainger, A. Difficulties in tracking the long-term global trend in tropical forest area. *Proce. Natl. Acad. Sci. USA* **2008**, *105*, 818–823. [[CrossRef](#)] [[PubMed](#)]
33. Saatchi, S.S.; Harris, N.L.; Brown, S.; Lefsky, M.; Mitchard, E.T.; Salas, W.; Zutta, B.R.; Buermann, W.; Lewis, S.L.; Hagen, S. Benchmark map of forest carbon stocks in tropical regions across three continents. *Proc. Natl. Acad. Sci. USA* **2011**, *108*, 9899–9904. [[CrossRef](#)] [[PubMed](#)]
34. Huete, A.R.; Didan, K.; Shimabukuro, Y.E.; Ratana, P.; Saleska, S.R.; Hutyra, L.R.; Yang, W.; Nemani, R.R.; Myneni, R. Amazon rainforests green-up with sunlight in dry season. *Geophys. Res. Lett.* **2006**, *33*, L06405. [[CrossRef](#)]

35. Guan, K.; Pan, M.; Li, H.; Wolf, A.; Wu, J.; Medvigy, D.; Caylor, K.K.; Sheffield, J.; Wood, E.F.; Malhi, Y. Photosynthetic seasonality of global tropical forests constrained by hydroclimate. *Nat. Geosci.* **2015**, *8*, 284. [[CrossRef](#)]
36. Liu, J.; Bowman, K.W.; Schimel, D.S.; Parazoo, N.C.; Jiang, Z.; Lee, M.; Bloom, A.A.; Wunch, D.; Frankenberg, C.; Sun, Y. Contrasting carbon cycle responses of the tropical continents to the 2015–2016 El Niño. *Science* **2017**, *358*, eaam5690. [[CrossRef](#)] [[PubMed](#)]
37. Harris, I.; Jones, P.D.; Osborn, T.J.; Lister, D.H. Updated high-resolution grids of monthly climatic observations—the CRU TS3.10 Dataset. *Int. J. Climatol.* **2014**, *34*, 623–642. [[CrossRef](#)]
38. Duncan, B.N.; Prados, A.I.; Lamsal, L.N.; Liu, Y.; Streets, D.G.; Gupta, P.; Hilsenrath, E.; Kahn, R.A.; Nielsen, J.E.; Beyersdorf, A.J. Satellite data of atmospheric pollution for US air quality applications: Examples of applications, summary of data end-user resources, answers to FAQs, and common mistakes to avoid. *Atmos. Environ.* **2014**, *94*, 647–662. [[CrossRef](#)]
39. Wahr, J.; Swenson, S.; Zlotnicki, V.; Velicogna, I. Time-variable gravity from GRACE: First results. *Geophys. Res. Lett.* **2004**, *31*, L11501. [[CrossRef](#)]
40. Save, H.; Bettadpur, S.; Tapley, B.D. High-resolution CSR GRACE RL05 mascons. *J. Geophys. Res. Solid Earth* **2016**, *121*, 7547–7569. [[CrossRef](#)]
41. Wayne, C.P. Meteorological drought. *Res. Pap.* **1965**, *45*, 58.
42. Karl, T.R.; Quayle, R.G. The 1980 summer heat wave and drought in historical perspective. *Mon. Wea. Rev.* **1981**, *109*, 2055–2073. [[CrossRef](#)]
43. Wells, N.; Goddard, S.; Hayes, M.J. A self-calibrating Palmer drought severity index. *J. Clim.* **2004**, *17*, 2335–2351. [[CrossRef](#)]
44. Van der Schrier, G.; Barichivich, J.; Briffa, K.; Jones, P. A scPDSI-based global data set of dry and wet spells for 1901–2009. *J. Geophys. Res. Atmos.* **2013**, *118*, 4025–4048. [[CrossRef](#)]
45. Crisp, D.; Pollock, H.R.; Rosenberg, R.; Chapsky, L.; Lee, R.A.; Oyafuso, F.A.; Frankenberg, C.; O'Dell, C.W.; Bruegge, C.J.; Doran, G.B. The on-orbit performance of the Orbiting Carbon Observatory-2 (OCO-2) instrument and its radiometrically calibrated products. *Atmos. Meas. Tech.* **2017**, *10*, 59–81. [[CrossRef](#)]
46. O'Dell, C.; Connor, B.; Bösch, H.; O'Brien, D.; Frankenberg, C.; Castano, R.; Christi, M.; Eldering, A.; Fisher, B.; Gunson, M. The ACOS CO₂ Retrieval Algorithm—Part 1: Description and Validation Against Synthetic Observations. *Atmos. Meas. Tech.* **2012**, *5*, 99–121.
47. Köhler, P.; Guanter, L.; Joiner, J. A Linear Method for the Retrieval of Sun-Induced Chlorophyll Fluorescence from GOME-2 and SCIAMACHY Data. *Atmos. Meas. Tech.* **2015**, *8*, 2589–2608. [[CrossRef](#)]
48. Joiner, J.; Yoshida, Y.; Guanter, L.; Middleton, E.M. New methods for the retrieval of chlorophyll red fluorescence from hyperspectral satellite instruments: Simulations and application to GOME-2 and SCIAMACHY. *Atmos. Meas. Tech.* **2016**, *9*, 3939–3967. [[CrossRef](#)]
49. Duysens, L.; Sweers, H. *Mechanism of the Two Photochemical Reactions in Algae as Studied by Means of Fluorescence*; Miyachi, S.: Tokyo, Japan, 1963; pp. 353–372.
50. Walther, S.; Guanter, L.; Heim, B.; Jung, M.; Duveiller, G.; Wolanin, A.; Sachs, T. Assessing the dynamics of vegetation productivity in circumpolar regions with different satellite indicators of greenness and photosynthesis. *Biogeosciences* **2018**, *15*, 6221–6256. [[CrossRef](#)]
51. Cox, P.M.; Pearson, D.; Booth, B.B.; Friedlingstein, P.; Huntingford, C.; Jones, C.D.; Luke, C.M. Sensitivity of tropical carbon to climate change constrained by carbon dioxide variability. *Nature* **2013**, *494*, 341. [[CrossRef](#)]
52. Qiu, B.; Xue, Y.; Fisher, J.B.; Guo, W.; Berry, J.A.; Zhang, Y. Satellite Chlorophyll Fluorescence and Soil Moisture Observations Lead to Advances in the Predictive Understanding of Global Terrestrial Coupled Carbon-Water Cycles. *Glob. Biogeochem. Cycles* **2018**, *32*, 360–375. [[CrossRef](#)]
53. Keppel-Aleks, G.; Wolf, A.S.; Mu, M.; Doney, S.C.; Morton, D.C.; Kasibhatla, P.S.; Miller, J.B.; Dlugokencky, E.J.; Randerson, J.T. Separating the influence of temperature, drought, and fire on interannual variability in atmospheric CO₂. *Glob. Biogeochem. Cycles* **2014**, *28*, 1295–1310. [[CrossRef](#)] [[PubMed](#)]
54. Keenan, T.; Baker, I.; Barr, A.; Ciais, P.; Davis, K.; Dietze, M.; Dragoni, D.; Gough, C.M.; Grant, R.; Hollinger, D. Terrestrial biosphere model performance for inter-annual variability of land-atmosphere CO₂ exchange. *Glob. Chang. Biol.* **2012**, *18*, 1971–1987. [[CrossRef](#)]
55. Lopes, A.P.; Nelson, B.W.; Wu, J.; de Alencastro Graça, P.M.L.; Tavares, J.V.; Prohaska, N.; Martins, G.A.; Saleska, S.R. Leaf flush drives dry season green-up of the Central Amazon. *Remote Sens. Environ.* **2016**, *182*, 90–98. [[CrossRef](#)]

56. Wu, J.; Albert, L.P.; Lopes, A.P.; Restrepo-Coupe, N.; Hayek, M.; Wiedemann, K.T.; Guan, K.; Stark, S.C.; Christoffersen, B.; Prohaska, N. Leaf development and demography explain photosynthetic seasonality in Amazon evergreen forests. *Science* **2016**, *351*, 972–976. [[CrossRef](#)]
57. Qiu, B.; Guo, W.; Xue, Y.; Dai, Q. Implementation and evaluation of a generalized radiative transfer scheme within canopy in the soil-vegetation-atmosphere transfer (SVAT) model. *J. Geophys. Res. Atmos.* **2016**, *121*, 12145–12163. [[CrossRef](#)]
58. Betts, R.A.; Jones, C.D.; Knight, J.R.; Keeling, R.F.; Kennedy, J.J.; Wiltshire, A.J.; Andrew, R.M.; Aragão, L.E. A successful prediction of the record CO₂ rise associated with the 2015/2016 El Niño. *Philos. Trans. R. Soc. Biol. Sci.* **2018**, *373*, 20170301. [[CrossRef](#)]
59. Laan-Luijkx, I.; Velde, I.; Krol, M.; Gatti, L.; Domingues, L.; Correia, C.; Miller, J.; Gloor, M.; Leeuwen, T.; Kaiser, J. Response of the Amazon carbon balance to the 2010 drought derived with CarbonTracker South America. *Glob. Biogeochem. Cycles* **2015**, *29*, 1092–1108. [[CrossRef](#)]
60. Doughty, C.E.; Goulden, M.L. Are tropical forests near a high temperature threshold? *J. Geophys. Res. Biogeosci.* **2008**, *113*, G00B07. [[CrossRef](#)]
61. Yang, J.; Tian, H.; Pan, S.; Chen, G.; Zhang, B.; Dangal, S. Amazon drought and forest response: Largely reduced forest photosynthesis but slightly increased canopy greenness during the extreme drought of 2015/2016. *Glob. Chang. Biol.* **2018**, *24*, 1919–1934. [[CrossRef](#)]
62. Koren, G.; van Schaik, E.; Araújo, A.C.; Boersma, K.F.; Gärtner, A.; Killaars, L.; Kooreman, M.L.; Kruijt, B.; van der Laan-Luijkx, I.T.; von Randow, C. Widespread reduction in sun-induced fluorescence from the Amazon during the 2015/2016 El Niño. *Philos. Trans. R. Soc. Biol. Sci.* **2018**, *373*, 20170408. [[CrossRef](#)] [[PubMed](#)]
63. Wang, X.; Piao, S.; Ciais, P.; Friedlingstein, P.; Myneni, R.B.; Cox, P.; Heimann, M.; Miller, J.; Peng, S.; Wang, T. A two-fold increase of carbon cycle sensitivity to tropical temperature variations. *Nature* **2014**, *506*, 212. [[CrossRef](#)] [[PubMed](#)]
64. Luo, X.; Keenan, T.F.; Fisher, J.B.; Jiménez-Muñoz, J.-C.; Chen, J.M.; Jiang, C.; Ju, W.; Perakalapudi, N.-V.; Ryu, Y.; Tadić, J.M. The impact of the 2015/2016 El Niño on global photosynthesis using satellite remote sensing. *Philos. Trans. R. Soc. Biol. Sci.* **2018**, *373*, 20170409. [[CrossRef](#)] [[PubMed](#)]



© 2019 by the authors. Licensee MDPI, Basel, Switzerland. This article is an open access article distributed under the terms and conditions of the Creative Commons Attribution (CC BY) license (<http://creativecommons.org/licenses/by/4.0/>).